Ferroelectricity in the multiferroic hexagonal manganites

Martin Lilienblum,[1] Thomas Lottermoser,[1] Sebastian Manz,[1] Sverre M. Selbach,[2] Andres Cano[3] and Manfred Fiebig[1]

[1]*Department of Materials, ETH Zurich, Vladimir-Prelog-Weg 4, 8093 Zurich, Switzerland*

[2]*Department of Materials Science and Engineering, NTNU, N-7491 Trondheim, Norway*

[3]*CNRS, Université de Bordeaux, ICMCB, UPR 9048, F-33600 Pessac, France*

Since their discovery in 1963 the hexagonal manganites have consolidated their role as exotic ferroelectrics with astonishing functionalities. Their introduction as room-temperature device ferroelectric[1] was followed by observations of giant flexoelectricity[2], multiferroicity with magnetoelectric domain and domain-wall coupling[3,4], protected vortex domain structures[5,6], topological domain-scaling behaviour[7] and domain walls with tunable conductance[8] and magnetism[9]. Even after half a century, however, the emergence of the ferroelectric state is a subject of fierce debates. We resolve the interplay of electric polarization, topological trimerization and temperature by direct access to the polarization up to 1400 K. Nonlinear optical experiments and piezoresponse force microscopy, complemented by Monte-Carlo simulations, reveal a single phase transition with ferroelectricity determined by topology rather than electrostatics. Fundamental properties of the hexagonal manganites, including an explanation for the two-phase-transition controversy as a finite-size scaling effect, are derived from this and highlight why improper ferroelectrics are an inherent source of novel functionalities.

The emergence of the spontaneous polarization in the hexagonal RMnO$_3$ system (R = Sc, Y, In, Dy - Lu) is one of the singular properties and, at the same time, one of the greatest mysteries of this class of compounds. Taking YMnO$_3$ as reference compound for the series (see Methods), Curie temperatures inexplicably spreading from 910 K to 1250 K have been reported[10–16,18,19]. In some of these cases ferroelectricity has been claimed to emerge together with a trimerizing lattice distortion in a single-step transition[16,18,19]. In other cases these two features have been proposed to occur separately[10–15]. On the theoretical side, the two-transition scenario has initially been supported by density-functional-theory calculations[20]. A more detailed analysis, however, suggests improper ferroelectricity triggered by the lattice trimerization in a single-step transition[21,22], in which secondary anomalies are yet possible due to the breaking of residual symmetries[23]. Direct measurement of the spontaneous polarization as function of temperature would clarify this puzzling situation. This was done once in a pyrocurrent measurement which pointed to an onset of ferroelectricity at 933 K[16]. All attempts to reproduce this experiment failed, however. Thus, in spite of 50 years of research, the emergence of the polar order in the hexagonal RMnO$_3$ multiferroics is surrounded by contradictions. This uncertainty extends to the universality class of this ferroelectric transition, as this basic question depends on the precise nature of the state undergoing the polar instability. The universality class and the corresponding critical behavior determines important physical properties from the macro- to the nanoscale. Understanding such functionalities is infinitely more difficult if the emergence of the ferroelectric order itself is unclear. Thus, for putting the intense research on the unusual properties of ferroelectric order in the hexagonal RMnO$_3$ system[2,3,5,8,9] onto a solid basis, this situation must be resolved.

Here we present nonlinear optical experiments in which the electromagnetic field of a frequency-doubled light wave couples directly and linearly to the spontaneous polarization of $YMnO_3$. They reveal a polarization emerging at $T_C \simeq 1259$ K with a subdued increase in amplitude showing no anomalies or discontinuities. Piezoresponse force microscopy (PFM) confirms that the ferroelectric domain pattern is seeded right below T_C. Monte-Carlo simulations reveal how topologically created vortex-like defects in the MnO_5 tilt pattern determine the ferroelectric state and many of its unusual properties. In particular, we show that the "second transition" below T_C is not associated to a phase transition, but caused by a finite-size scaling effect.

At room temperature, the spontaneous polarization $P_s = 5.6\ \mu$C/cm^2 of $YMnO_3$ is observed together with unit-cell-trimerizing tilts of the MnO_5 bipyramids and Y displacements along the c axis. The tilt is parameterized[22,23] by the observable amplitude Q and angle Φ in Fig. 1a. The resulting domains typically form three-dimensional patterns with vortex-like meetings of all six possible domain states[5]. These vortices are topologically protected; they and the associated domains cannot be destroyed by electric-field poling[6].

An established method for probing ferroelectric order is second harmonic generation (SHG): emission of light at frequency 2ω from a crystal irradiated with light at frequency ω. In the leading order, a SHG signal $I_{\mathrm{SHG}} \propto |\mathbf{E}(2\omega)|^2$ is observed only if inversion symmetry is broken[24], e.g. by a ferroelectric polarization P_s as in $YMnO_3$. SHG can thus probe P_s directly with linear coupling $\mathbf{E}(2\omega) \propto P_s$. In addition, SHG measurements are highly sensitive with a detection limit down to[25] < 1 nCcm^{-2} and they are performed contact-free and thus not obstructed by artifacts from

contact resistance or increased leakage at high temperature. Since SHG has never been used for probing ferroelectric order at temperatures > 1000 K we first scrutinized the relation between the SHG amplitude and the spontaneous polarization of ferroelectrics in this range. These reference experiments and various error sources in SHG are discussed in the Supplementary Material. All our tests confirm that $\mathbf{E}(2\omega)$ in $YMnO_3$ is scaling exclusively with P_s up to at least 1400 K.

Figure 1b shows the temperature dependence of the SHG amplitude of $YMnO_3$ up to 1400 K. Dilatometric measurements on the sample reveal a transition temperature of (1266 ± 5) K. The SHG amplitude shows a gradual and continuous decrease towards this value. Fitting $P_s \propto (T_C - T)^{\beta_{P_s}}$ above 600 K reveals a transition at $T_C = (1259 \pm 24)$ K and $\beta_{P_s} = 2.04 \pm 0.12$. This temperature dependence is strikingly different from that extrapolated from other measurements[10,16], and there is no sign of any secondary anomaly.

In order to understand the emergence of ferroelectricity on a local scale, we then applied piezoresponse force microscopy (PFM). Figure 2 shows the ferroelectric domain pattern at room-temperature *before* and *after* heating the sample to 1230 K ($\lesssim T_C$) and 1270 K ($\gtrsim T_C$). After the cycle through 1230 K the observed changes are minimal even though the spontaneous polarization P_s drops to 0.7% according to the fit in Fig. 1b. In contrast, after the cycle through 1270 K, the pattern and the size of the domains[7] are completely different. The similarity of Figs. 2a and 2b hence reveals that the distribution of ferroelectric domains is predetermined by some primary order parameter that is already large at 1230 K. Here, the trimerization order parameter (Q, Φ) is a likely candidate.

We therefore scrutinize the temperature dependence of Q and Φ and their the relation to P_s by Monte-Carlo (MC) simulations. For this, we consider a discrete six-state clock model[26] on a three-dimensional hexagonal lattice as in Ref. 27. This model is derived directly from the general expression for the free energy of the hexagonal manganite series used in Landau theory[22,23]. It represents the strong-coupling limit of a continuous XY model in which the coupling between Q and P_s generates the Z_6 anisotropy terms that allow us to introduce the six-state clock model[23]. The clock variable $s_j = e^{i\phi_j}$ is associated to the trimerization states ($\phi_j = n_j \cdot 60^\circ$ with $n_j = 0, 1, \ldots 5$). The secondary variable $p_j = \cos(3\phi_j)$ represents the electric polarization so that $p_j = \pm 1$ becomes an Ising-like variable at each lattice site j. As customary in MC simulations, the macroscopic quantities Q and P_s are obtained from the statistical average of the microscopic variables s_j and p_j respectively. Details on the relation between the "physical" XY model for the hexagonal $R\mathrm{MnO_3}$ system and the clock model and on the technical aspects of the Monte-Carlo simulations are given in Methods.

The resulting temperature dependencies are shown in Fig. 3. The computed polarization P_s bears an extraordinary resemblance to the measured data (see Fig. 2), and in fact is described by the same critical exponent $\beta_{P_s} = 2.00 \pm 0.02$. In contrast, Q shows a steep increase below T_C. This is well described by the critical exponent $\beta_Q = 0.348$ as in the XY universality class, which confirms the emergent continuous $U(1)$ symmetry of our model. The six-fold anisotropy becomes relevant away from T_C and eventually establishes the discrete Z_6 symmetry. We thus investigate the "discreteness parameter" $\Phi_6 = \langle \cos(6\phi) \rangle$, which becomes different from 0 when the average phase ϕ is distributed in a discrete fashion. As we see in Fig. 3, Φ_6 reveals that the emergent $U(1)$

symmetry is effectively preserved only within the interval $T_C^* \lesssim T \leq T_C$.

The role of T_C^* is further highlighted by Fig. 4, which shows MC snapshots of non-thermalized distributions of the six clock states and the associated projection onto two polarization states. At $T > T_C^*$, polarization domains are not yet visible, which is in agreement with the Φ_6 behaviour in Fig. 3. We note, however, a non-random distribution of ϕ_j as soon as $T < T_C$. This is quantified by the local value $\overline{q}_j e^{i\overline{\phi}_j}$ obtained by averaging locally across a small number of sites in the MC lattice (see Methods). We see that $\overline{\phi}_j$ varies continuously throughout the sample and, in particular, around vortex cores that are already visible without domains. In contrast, at $T < T_C^*$ the familiar domain pattern with six domain states of either polarization and discrete values of $\overline{\phi}_j$ has been established. Note that the continuous distribution of $\overline{\phi}_j$ at $T_C^* \lesssim T \lesssim T_C$ predetermines the ferroelectric domain structure below T_C^* and preserves it in heating cycles close to (but always below) T_C. This was verified in a MC heating cycle and explains the similarity of the domain structures in Figs. 2a and 2b.

The MC simulations thus provide additional insight into the local nature of the trimerization transition. Continuous vortices with smooth variations of the trimerization angle Φ are topologically created when going below T_C. At T_C^* they evolve into discrete vortices of ferroelectric domains upon further cooling[7]. Since topology rather than electrostatics determines their formation, their distribution is isotropic and statistical, and they turn out to be quite immobile (see Figs. 2 and 4). The emergence of the ferroelectric domains is predestinated by the continuous vortices. For example, the vortex section with $-30^\circ < \overline{\phi}_j < 30^\circ$ at high temperature will preferentially convert

into the ferroelectric domain state with $\overline{\phi}_j = 0$ at low temperature, as Fig. 4 indicates[22].

Importantly, the MC simulation offers a natural explanation for the two-phase-transition controversy in the literature and the large spread in values reported for T_C. As can be seen in Fig. 3, criticality in our system is displayed differently by Q and Φ. Whereas Q emerges right at T_C, Φ locks into discrete values in a range centered around $T_C^* < T_C$. This is a finite-size scaling effect related to the universality class of the six-state clock model[28]. It is associated to the length scale $\xi_\Phi \sim |T - T_C|^{-\nu_\Phi}$ diverging faster than the length scale $\xi_Q \sim |T - T_C|^{-\nu_Q}$ ($\nu_\Phi/\nu_Q > 1$). In order to recognize long-range order for Q and Φ and separate it from mere statistical fluctuations of these parameters we thus require the temperatures T_C^* and T_C, respectively, for a system of finite size L with T_C^* approaching T_C for $L \to \infty$. Thus, T_C^* is caused by a finite-size effect. This is *not* a consequence of sample inhomogeneity, however: Even in perfectly homogeneous $YMnO_3$ samples the perception of the long-range order in an experiment is determined by the coherence length L of the technique that is employed to probe the system and, furthermore, on the explicit dependence of the experimental observable on Q and Φ. Even though the actual phase transition temperature is T_C, an experimental probe may therefore simulate an apparent secondary transition at T_C^*. The only real phase transition temperature, however, is T_C. The actual order parameter of the ferroelectric state, P_s, only shows a single transition at T_C in the MC simulations. This is mirrored by the SHG measurement because SHG probes P_s directly. In addition P_s and, hence, SHG are only weakly dependent on L (see Supplementary Fig. S2) and thus largely insensitive to the finite-size scaling effects a more indirect probing technique would suffer from.

This perfectly explains the long-standing "two-phase-transition controversy" and the apparent discrepancy between, for example, neutron diffraction experiments and the present results. Specifically, the concomitant loss of long-range structural coherence above T_C^* is not easily captured by reciprocal space diffraction. This meso-scale disorder does not hamper the SHG measurements and, as mentioned, the system size dependence of SHG is very weak.

In summary, the interplay of electric polarization, topological trimerization and temperature was resolved for the multiferroic ferroelectric $YMnO_3$. SHG couples directly to the spontaneous polarization and reveals its emergence at $T_C = 1259$ K, i.e., in a single transition along with the unit-cell-trimerizing lattice distortion. PFM and MC simulations reveal an isotropic network of trimerization vortices around which, sufficiently close to T_C, the trimerization phase varies in a continuous fashion. The temperature $T_C^* < T_C$ around which the lock-in of the trimerization into discrete polarization states becomes observable depends on the coherence length of the experimental probe that is applied. This explains claims of a "second transition". The distribution of the six trimerization states and the corresponding ferroelectric domains is seeded by the network of continuous vortices near T_C. Their distribution is determined by topology rather than electrostatics which explains the isotropic distribution of the ferroelectric domains in this anisotropic crystal and the presence of unfavorable ferroelectric domain walls perpendicular to the polarization and with highly anisotropic conductance.

Our work thus explains some of the most puzzling aspects of ferroelectricity in the hexagonal manganites, and five decades of contradictory results are resolved into a coherent overall

picture of dielectric long-range order in this system. This will prove indispensable in the continuing exploration of magneto-dielectric functionalities in this archetypal class of multiferroics with independent magnetic and ferroelectric order. It furthermore highlights that improper ferroelectrics are an inherent source of novel functionalities. If properties other than the dielectric ones determine the manifestation of ferroelectric order, domain configurations normally avoided may occur and entail exotic behavior within the domains and at the domain walls, like in the hexagonal RMnO$_3$ compounds.

Acknowledgements This work was supported by the ETH Research Grant No. ETH-06 12-2. The authors thank Nicola A. Spaldin for enlightening discussions.

Author contributions M. L. performed the SHG and PFM experiments, T. L. performed the Monte-Carlo simulations, S. M. performed the pyrocurrent measurements. S. M. S. performed the dilatometry measurements. A. C. contributed to the discussion and analysis. M. F. supervised the work.

Competing Interests The authors declare that they have no competing financial interests.

Correspondence Correspondence and requests for materials should be addressed to M. L. (email: martin.lilienblum@mat.ethz.ch).

Methods

Samples and setup: The entire hexagonal RMnO$_3$ series (R = Sc, Y, In, Dy - Lu) displays trimerization-driven ferroelectric order with the radius of the R ions correlating to the Curie temperature[29]

(the magnetic difference between the rare-earth and transition-metal ions manifests in the magnetic properties below the Néel temperature of $\sim$ 100 K only). We therefore chose the most intensely investigated compound, $YMnO_3$, as our reference compound for the series. $YMnO_3$ single-crystals grown by the floating-zone technique were cut and polished into platelets with in-plane orientation of the spontaneous polarization and a thickness from 30 to 90 μm. For temperature control the sample is placed either in a cryostat or a split-tube furnace. This allowed us to cover the entire range in two uninterrupted scans from 100 K to 400 K and from 400 K to 1400 K. The furnace is purged with N_2 in order to promote chemical self-poling[30] which brings the sample close to a single-domain polarization state as we verified in PFM scans. This minimizes destructive interference of SHG contributions from opposite domain states[31] and thus maximizes the SHG yield. Manganites are known to for their sensitivity to stoichiometry, and the resulting fluctuations of the valence state could affect the phase transition investigated in our work. Here, thermogravimetric studies[17] have shown that $YMnO_3$ can only accomodate a small oxygen deficiency of delta=0.037 at 1473 K. In line with this, our high-temperature x-ray diffraction studies in N_2 and O_2 across the ferroelectric transition of $YMnO_3$ and $HoMnO_3$ did not reveal differences in crystal structure or the manganese valence state.[18]

For SHG we used 120-fs laser pulses of $\sim$ 150 μJ emitted at 1 kHz repetition rate from a frequency-tunable fs-laser system. As detailed in Ref. 3, the frequency-doubled light was generated in transmission via the susceptibilities χ_{zzz}, χ_{zxx}, and χ_{xxz}. As SHG photon energy we chose 1.96 eV, where the SHG susceptibilities are reasonably large[3] and black-body radiation from the heated sample is negligible.

PFM was carried out as detailed in Ref. 34. Here chemical self poling had to be avoided so that annealing experiments were were performed under O_2 atmosphere. Annealing to temperatures above ~ 1000 K induced a surface reconstruction with a rms roughness of typically 5 nm. We thus polished the samples after completion of the annealing cycle in order to re-establish proper PFM imaging conditions.

Monte-Carlo (MC) simulations:

Our model is based on the general expression for the free energy of the hexagonal $R\mathrm{MnO_3}$ series obtained from group theoretical considerations[21–23] and confirmed by DFT.[22] More specifically, DFT reveals that the K_3 mode nearly displays a continuous $U(1)$ symmetry (see Ref. 22 for the specific case of $\mathrm{YMnO_3}$, although the same holds for the rest of the family). Thus, one can initially consider the XY model

$$H = -J \sum_{\langle i,j \rangle} \cos\left(\phi_i - \phi_j\right), \tag{1}$$

where complex variables $s_j = e^{i\phi_j}$ are associated to the local K_3 distortions. At this level, the angle ϕ_j can take any value between 0 and 2π at each site $j = 1 \ldots L^3$ of the lattice of lateral extension L. However, DFT also shows that the coupling between the K_3 mode and the polarization (Γ_2^-) plays a crucial role, as it eventually generates a strong Z_6 anisotropy in the K_3 sector that determines the actual trimerized states that are realized experimentally. In terms of the XY model this coupling reads $H_{\mathrm{int}} = -g \sum_j p_j \cos(3\phi_j)$, where p_j is the (local) polarization. We make use of these DFT results for $\mathrm{YMnO_3}$ and restrict the angle ϕ_j to $\phi_j = n_j \cdot 60^\circ$ ($0 \leq n_j \leq 5$) in our MC simulations. Effectively, we thus introduce a six-state clock model. We formally integrate

the electric polarization and consider the "strong coupling limit" revealed by DFT. The electric polarization then becomes an Ising-like variable: $p_j \propto \cos(3\phi_j) = \pm 1$.

The MC simulations were performed by application of a hybrid algorithm combining a parallelized implementation of the standard Metropolis algorithm[32] and an adapted version of the Wolff cluster algorithm[33]. As customary in MC simulations, the macroscopic order parameter is obtained as $Q = \langle |q| \rangle = \langle |qe^{i\phi}| \rangle$, where $\langle \ldots \rangle$ denotes the statistical MC average and $qe^{i\phi} \equiv L^{-3} \sum_j s_j$. The electric polarization is derived from the MC simulation as $P_s = \langle |p| \rangle$ where $p = L^{-3} \sum_j p_j$ with the Ising variable $p_j = \cos(3\phi_j)$. Thus, the six clock states are projected onto two polarization states.

For determining the temperature dependence of P_s, Q and Φ_6 we used a lattice with L^3 cells (with L as given in the figure captions). The relative temperature T/T_C was increased in steps of 0.033. At each temperature step multiple MC sweeps through the full lattice were performed. The initial sweeps were discarded to ensure thermal equilibration. Then Q, P_s and Φ_6 were derived as an average across the remaining MC sweeps.

Domain images were simulated by a non-equilibrium temperature run on the three-dimensional lattice. For this calculation, the temperature was decreased from $T = 1.2 \cdot T_C$ in steps of $6.8 \cdot 10^{-4}$, performing a single MC sweep at each step. The local phase $\overline{\phi}_j$ was calculated as average $\overline{q}_j e^{i\overline{\phi}_j} \equiv \ell^{-3} \sum_{j=1}^{\ell^3} s_j$ across a small small cube of extension $\ell \ll L$. Here we chose $\ell = 5$ and $L = 256$. All the MC-simulated domain images show a cross-section in the basal plane.

1. Fujimura, N., T. Ishida, T., T. Yoshimura, T. & Ito, T. Epitaxially grown $YMnO_3$ film: New candidate for nonvolatile memory devices. *Appl. Phys. Lett.* **69**, 1011 (1996).

2. Lee, D., Yoon, A., Jang, S. Y., Yoon, J.-G., Chung, J.-S., Kim, M., Scott, J. F. & Noh, T. W. Giant flexoelectric effect in ferroelectric epitaxial thin films. *Phys. Rev. Lett.* **107**, 057602 (2011).

3. Fiebig, M., Lottermoser, T., Fröhlich, D., Goltsev, A. V. & Pisarev, R. V. Observation of coupled magnetic and electric domains. *Nature* **419**, 818 (2002).

4. Lottermoser, T., Lonkai, T., Amman, U., Hohlwein, D., Ihringer, J. & Fiebig, M. Magnetic phase control by an electric field. *Nature* **430**, 541 (2004).

5. Choi, T., Horibe, Y., Yi, H. T., Choi, Y. J., WeidaWu & Cheong, S.-W. Insulating interlocked ferroelectric and structural antiphase domain walls in multiferroic $YMnO_3$. *Nature Mater.* **9**, 423 (2010).

6. Jungk, T., Hoffmann, Á., Fiebig, M., & Soergel, E. Electrostatic topology of ferroelectric domains in $YMnO_3$. *Appl. Phys. Lett.* **97**, 012904 (2010).

7. Griffin, S. M., Lilienblum, M., Delaney, K. T., Kumagai, Y., Fiebig, M., & Spaldin, N. A. Scaling behavior and beyond equilibrium in the hexagonal manganites. *Phys. Rev. X* **2**, 041022 (2012).

8. Meier, D., Seidel, J., Cano, A., Delaney, K., Kumagai, Y., Mostovoy, M., Spaldin, N. A., Ramesh, R. & Fiebig, M. Anisotropic conductance at improper ferroelectric domain walls. *Nature Mater.* **11**, 284 (2012).

9. Geng, Y., Lee, N., Choi, Y. J., Cheong, S.-W. & Wu, W. Collective magnetism at multiferroic vortex domain walls. *Nano Lett.* **12**, 6055 (2012).

10. Gibbs, A. S., Knight, K. S. & Lightfoot, P. High-temperature phase transitions of hexagonal $YMnO_3$. *Phys. Rev. B* **83**, 094111 (2011).

11. Katsufuji, T., Mori, S., Masaki, M., Moritomo, Y., Yamamoto, N., and Takagi H. Dielectric and magnetic anomalies and spin frustration in hexagonal $R MnO_3$ (R = Y, Yb, and Lu). *Phys. Rev. B* **64**, 104419 (2001).

12. Kim, J., Cho, K. C., Koo, Y. M., Hong, K. P. & Shin, N. YO hybridization in the ferroelectric transition of $YMnO_3$. *Appl. Phys. Lett.* **95**, 132901 (2009).

13. Nénert, G., Pollet, M., Marinel, S., Blake, G. R., Meetsma, A. & Palstra, T. T. M. Experimental evidence for an intermediate phase in the multiferroic $YMnO_3$. *J. Phys. Condens. Matter* **19**, 466212 (2007).

14. Tyson, T. A., Wu, T., Chen, H. Y., Bai, J., Ahn, K. H., Pandya, K. I., Kim, S. B. & Cheong, S.-W. Measurements and ab initio molecular dynamics simulations of the high temperature ferroelectric transition in hexagonal $RMnO_3$. *J. Appl. Phys.* **110**, 084116 (2011)

15. Thomson, R. I., Chatterji, T., Howard, C. J., Palstra, T. T. M. & Carpenter, M. A. Elastic anomalies associated with structural and magnetic phase transitions in single crystal hexagonal $YMnO_3$. *J. Phys.: Condens. Matter* **26**, 045901 (2014).

16. Ismailzade, I. G. & Kizhaev, S. A. Determination of the Curie point of the ferroelectric $YMnO_3$ and $YbMnO_3$. *Sov. Phys. Solid State* **7**, 236 (1965).

17. Kamata, K., Nakajima, T. & Nakamura T. Thermogravimetric study of rare-earth manganites $AMnO_3$ (A = Sm, Dy, Y, Er, Yb) at 1200C. *Mater. Res. Bull.* **14**, 1007 (1979).

18. Selbach, S. M., Løvik, A. N., Bergum, K., Tolchard, J. R., Einarsrud, M.-A. & Grande, T. Crystal structure, chemical expansion and phase stability of $HoMnO_3$ at high temperature. *J. Solid State Chem.* **196**, 528 (2012).

19. Jeong, I.-K., Hur, N. & Proffen, T. High-temperature structural evolution of hexagonal multiferroic $YMnO_3$ and $YbMnO_3$. *J. Appl. Cryst.* **40**, 730 (2007).

20. van Aken, B. B., Palstra, T. T. M., Filippetti, A., and Spaldin, N. A. The origin of ferroelectricity in magnetoelectric $YMnO_3$. *Nature. Mater.* **3**, 164 (2004)

21. Fennie, C. J. & Rabe, K. M. Ferroelectric transition in $YMnO_3$ from first principles. *Phys. Rev. B* **72**, 100103(R) (2005).

22. Artyukhin, S., Delaney, K. T., Spaldin, N. A. & Mostovoy, M. Landau theory of topological defects in multiferroic hexagonal manganites. *Nature Mater.* **13**, 42 (2014)

23. Cano, A. Hidden order in hexagonal $RMnO_3$ multiferroics (R=Dy – Lu, In, Y, and Sc). *Phys. Rev. B* **89**, 214107 (2014)

24. Denev, S. A., Lummen, T. T. A., Barnes, E., Kumar, A. & Gopalan, V. Probing ferroelectrics using optical second harmonic generation. *J. Am. Ceram. Soc.* **94**, 2699 (2011)

25. Leo, N., Meier, D., Pisarev, R. V., Lee, N., Cheong, S.-W. & Fiebig, M. Independent Ferroelectric Contributions and Rare-Earth-Induced Polarization Reversal in Multiferroic $TbMn_2O_5$. *Phys. Rev. B* **85**, 094408 (2012).

26. José, J. V., Kadanoff, L. P., Kirkpatrick, S. & Nelson, D. R. Renormalization, vortices, and symmetry-breaking perturbations in the two-dimensional planar model. *Phys. Rev. B* **16**, 1217 (1977).

27. Lin, S.-Z., Wang, X., Kamiya, Y., Chern, G.-W., Fan, F., Casas, B., Liu, Y., Kiryukhin, V., Zurek, W. H., Batista, C. D., & Cheong, S.-W., Topological defects as relics of emergent continuous symmetry and Higgs condensation of disorder in ferroelectrics. *Nature Phys.* **10**, 970 (2014).

28. Lou, J., Sandvik, A. W., Balents, L. Emergence of U(1) symmetry in the 3D XY model with Z_q anisotropy. *Phys. Rev. Lett.* **99**, 207203 (2007).

29. Chae, S. C., Lee, N., Horibe, Y., Tanimura, M., Mori, S., Gao, B., Carr, S. & Cheong, S.-W. Direct Observation of the proliferation of ferroelectric loop domains and vortex-antivortex pairs. *Phys. Rev. Lett.* **108**, 167603 (2012).

30. Chae, S. C., Horibe, Y., Jeong, D. Y., Rodan, S., Lee, N. & Cheong, S.-W. Self-organization, condensation, and annihilation of topological vortices and antivortices in a multiferroic. *Proc. Natl. Acad. Sci* **107**, 21366 (2010).

31. Fiebig, M., Fröhlich, D., Lottermoser, Th. & Maat, M. Probing of ferroelectric surface and bulk domains in ferroelectric RMnO$_3$ (R = Y, Ho) by second harmonic generation, *Phys. Rev. B* **66**, 144102 (2002).

32. Metropolis, N., Rosenbluth, A. W., Rosenbluth, M. N., Teller, A. H., Teller, E. Equation of state calculations by fast computing machines. *J. Chem. Phys.* **21**, 1087 (1953).

33. Wolff, U. Collective Monte Carlo updating in a high precision study of the $x - y$ model. *Nucl. Phys. B* **322**, 759 (1989).

34. Soergel, E. Piezoresponse force microscopy. *J. Phys. D: Appl. Phys.* **44**, 464003 (2011).

Figure 1 Direct probing of the spontaneous polarization by optical SHG. a, Ferroelectric order in hexagonal $YMnO_3$. The side and top views of the unit cell show the distribution of tilted MnO_5 bipyramids in the unit cell. The MnO_5 tilts can be parametrized as $\eta_1 \cos(\mathbf{q}\cdot\mathbf{r}) + \eta_2 \sin(\mathbf{q}\cdot\mathbf{r})$, where $\mathbf{q} = (1/3, 1/3, 0)$ is the trimerization wavevector and $(\eta_1, \eta_2) \equiv (Q\cos\Phi, Q\sin\Phi)$ the corresponding order parameter. Exemplarily, we show the associated displacement for one of the three bipyramids constituting the tilt. **b**, Temperature dependence of the SHG amplitude from the x-face of an $YMnO_3$ single crystal (data points) and power-law fit (red solid line) applied to the range above 600 K. Corroborated by the inset, the fit (red line) reveals a single transition at $T_C = (1259 \pm 24)$ K with no further phase transition or discontinuities and a critical exponent $\beta_{P_s} = 2.04 \pm 0.12$. Integrated pyrocurrent measurments (blue line) confirm the proportionality between the SHG amplitude and the spontaneous polarization. For comparison, all SHG datasets were scaled with respect to P_s. Data in the inset above 1150 K are not shown because they begin to scatter into the negative range so that $P_s^{0.5}$ can be no longer derived.

Figure 2 Effect of annealing on the ferroelectric domain structure. a, Room-temperature PFM scan of a region on the x-face of the $YMnO_3$ sample from Fig. 1. **b**, Room-temperature PFM scans of the same region after annealing to 1230 K close below T_C. The annealing has almost no effect on the domain pattern. **c**, Room-temperature PFM scans of the same region after annealing to 1270 K close above T_C. The domain pattern has changed completely. The higher density of the domains is related to the lower cooling rate during the annealing cycle[7].

Figure 3 MC simulation of the ferroelectric phase transition in $YMnO_3$. Temperature dependence of the spontaneous polarization P_s in comparison to the MnO_5 tilt parameter Q and the discreteness parameter Φ_6. The data were derived by a three-dimensional MC simulation of the six-state clock model for a lattice with $L = 64$ (Q and P_s) and $L = 16$ (Φ_6) as described in Methods. Lines show fits to the MC data.

Figure 4 Emergence of ferroelectric domains in $YMnO_3$. a, Spatial distribution of the six $YMnO_3$ clock states at $T/T_C = 0.9$ derived by a non-equilibrium MC simulation as in Fig. 3. **b**, Spatial distribution of the two polarization domain states calculated as projection from (a). **c**, Angular distribution of the local average value $\overline{\phi}_j$ of the azimuthal MnO_5 tilt across the sample. **d** – **f**, Like (a-c), but at $T/T_C = 0.1$. The distribution at $T/T_C = 0.9$ is dominated by vortex cores with a continuous variation of $\overline{\phi}_j$ around them whereas domains are absent and $P_s \approx 0$. Towards $T/T_C = 0.1$ this structure evolves into the familiar vortex-like ferroelectric domain pattern of $YMnO_3$.

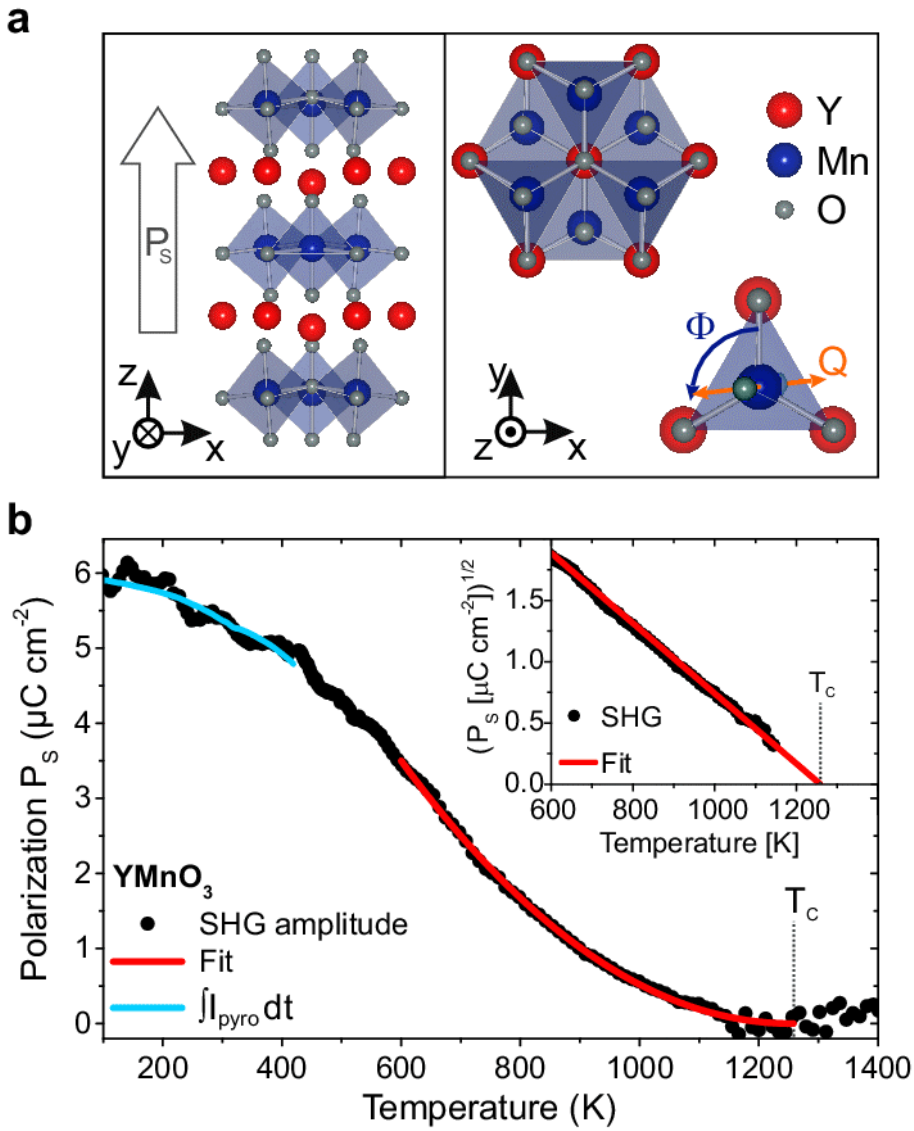
a
Y
Mn
O
P_S
z
y
x
y
z
x
Φ
Q
b
Polarization P_S (μC cm^{-2})
Temperature (K)
$YMnO_3$
SHG amplitude
Fit
$\int I_{pyro}\,dt$
T_C
$(P_S$ [μC cm^{-2}]$)^{1/2}$
SHG
Fit
Temperature [K]
T_C

Figure 1

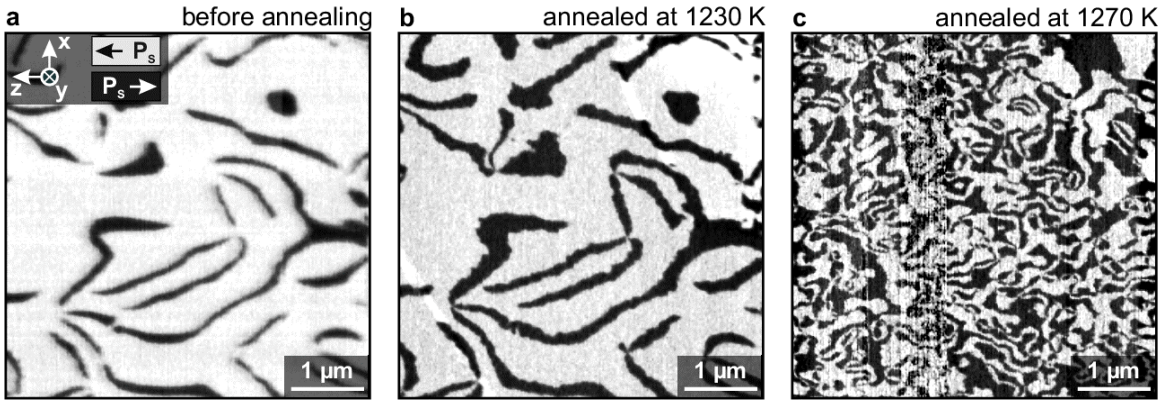
a
before annealing
b
annealed at 1230 K
c
annealed at 1270 K
x
z
y
P_s
P_s
1 µm
1 µm
1 µm

Figure 2

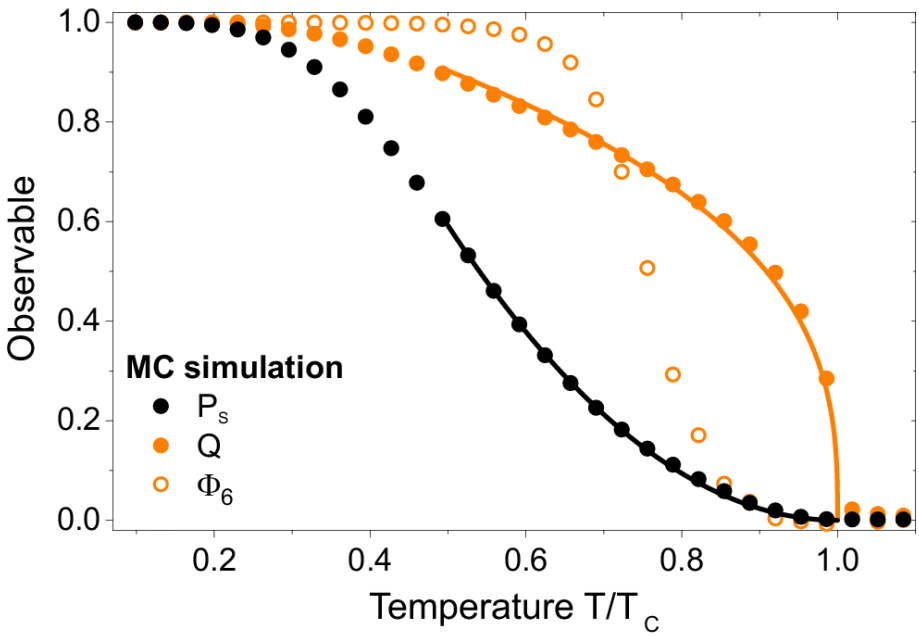
Observable
1.0
0.8
0.6
0.4
0.2
0.0
MC simulation
P_s
Q
Φ_6
0.2
0.4
0.6
0.8
1.0
Temperature T/T_C

Figure 3

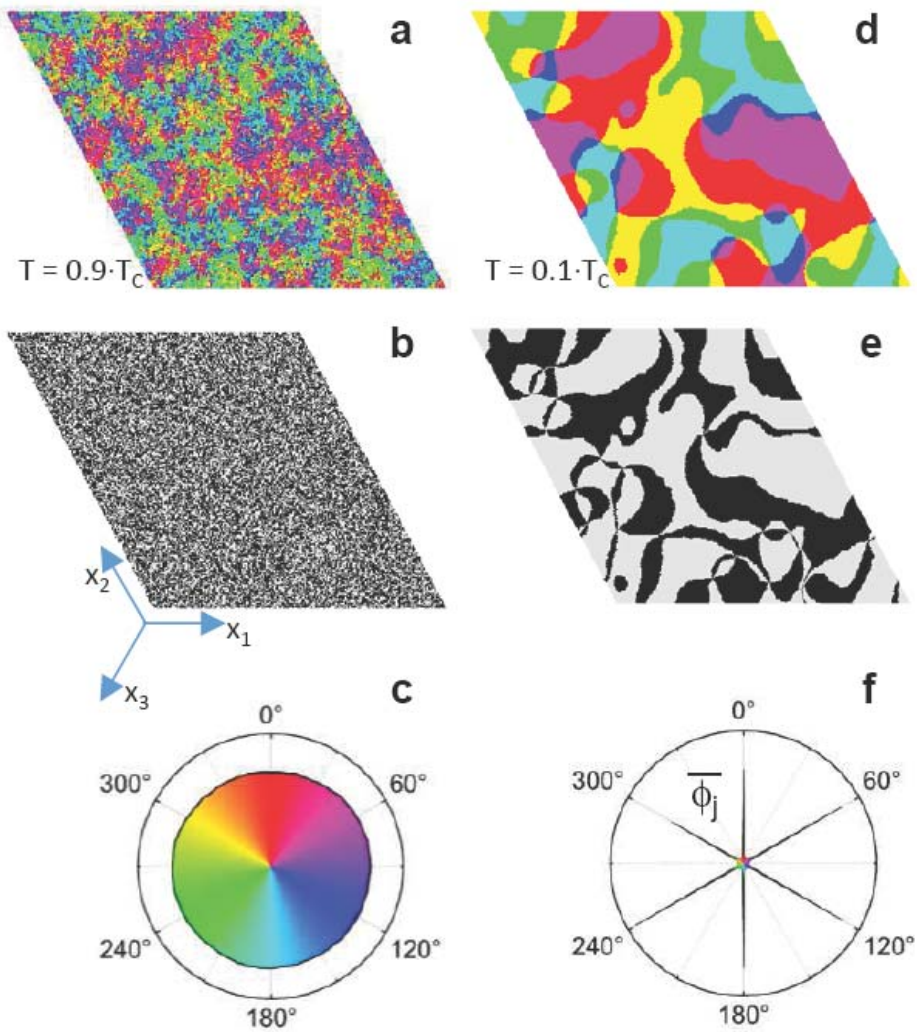

Figure 4

Supplementary Information: Ferroelectricity in the multiferroic hexagonal manganites

Martin Lilienblum,[1] Thomas Lottermoser,[1] Sebastian Manz,[1] Sverre M. Selbach,[2] Andres Cano[3] and Manfred Fiebig[1]

[1]*Department of Materials, ETH Zurich, Vladimir-Prelog-Weg 4, 8093 Zurich, Switzerland*

[2]*Department of Material Science and Engineering, NTNU, N-7491 Trondheim, Norway*

[3]*CNRS, Université de Bordeaux, ICMCB, UPR 9048, F-33600 Pessac, France*

1 High-temperature SHG measurements on ferroelectrics

SHG has never been used for probing ferroelectric order at temperatures as high as 1400 K. At first, we therefore verified the relation between the SHG amplitude and the spontaneous polarization P_s on $LiNbO_3$, an archetypal ferroelectric with a Curie temperature $T_C = 1403$ K[1]. For this intensely investigated ferroelectric it is well established that the spontaneous polarization P_s follows the classical relation $P_s \propto (T_C - T)^{0.5}$ obtained from Landau theory[2]. Figure S1 shows the temperature dependence of the SHG amplitude on a bulk single crystal of $LiNbO_3$ in comparison to this scaling law. The agreement is excellent, including the value $T_C = (1404 \pm 1)$ K. In this reference ferroelectric $\mathbf{E}(2\omega)$ is thus scaling exclusively with P_s across the entire temperature range. There is no "unspecific" decrease of the nonlinear conversion efficiency with temperature.

2 High-temperature SHG measurements on hexagonal $YMnO_3$

A variety of tests and reference measurements accompanied the determination of the temperature dependence of the spontaneous polarization of $YMnO_3$ by SHG.

- Figure 1a in the main text shows the SHG amplitude $|\mathbf{E}(2\omega)|$ for $YMnO_3$ in comparison to the spontaneous polarization obtained by an integrated pyrocurrent measurement. The experiment ranges from 100 K, below which SHG from the antiferromagnetic order interferes with the ferroelectric signal[3], to 400 K, above which the conductivity of the sample impedes pyrocurrent measurements. This range is large enough to reveal the correspondence between $|\mathbf{E}(2\omega)|$ and P_s, in contrast to a scaling with other order parameters such as Q, which would in addition be incompatible with symmetry.

- Repeated SHG-versus-temperature scans did not reveal any drifts as they might be caused by accumulating chemical or structural changes in the high-temperature environment.

- The temperature dependence of the linear transmission was taken into account by normalizing the SHG intensity accordingly.

- The frequency-tripled signal (3ω) is allowed at all temperatures without any order-parameter dependence. Up to 1400 K, we observed no decrease of the normalized THG intensity with temperature.

All these auxiliary experiments confirm that, in agreement with the reference measurement in Fig. S1, there is no “unspecific” decrease of nonlinear conversion efficiency with temperature. The SHG amplitude in Fig. 1b in the main text gives an accurate account of the spontaneous polarization in $YMnO_3$ up to 1400 K.

3 Error sources in SHG

Domain walls may lead to systematic errors in the relation between the SHG amplitude and the spontaneous polarization. Because of their lower symmetry the ferroelectric domain walls might lead to additional contributions to the SHG yield. In spatially resolved SHG experiments at room temperature, however, such contributions were not detected. Likewise, we excluded that shifts of the domain distribution with temperature affect the SHG yield. First, the PFM scans in Fig. 2 show that even very close to T_C the domains, respectively the underlying trimerization vortices, do not visibly move. Second, self-poling towards a single-domain state as mentioned in Methods suppresses the effect of destructive interference of SHG contributions from opposite domains in the first place.

Aside from domain walls, the reduced symmetry at the sample surface can lead to a SHG background signal not coupling to the spontaneous polarization[4]. Such contributions would be equally present above and below T_C. Their contribution is negligible according to the SHG data in Fig. 1b.

On the other hand, the sensitivity of SHG is limited when it comes to non-polar phase

transitions. Violation of inversion symmetry is required for obtaining the leading-order electric dipole contribution to SHG[4,5]. In the non-polar phase higher-order magnetic-dipole or electric-quadrupole contributions are allowed but, according to the absence of a SHG signal above T_C, to weak to be detected. Thus, any non-polar phase transitions that might occur *above* the trimerization temperature are not resolved by our SHG experiments. Likewise, isosymmetric phase transitions below T_C would not lead to new polarization components in the SHG signal. Yet probably, the intensity of the already existing components are changed by such a transformation so that an isosymmetric phase transitions would be resolved by SHG after all. No such transition was detected, however.

4 Coherence length in the SHG measurements

A main result of this work is that the perception of long-range order the RMnO$_3$ system depends crucially on the coherence length of the experimental technique that is employed to probe the system. As explained in the main text, this is *not* a consequence of sample inhomogeneity (like nano-clustering or a relaxor-like structure) but of the amount of sample volume that is required to recognize long-range order. In this respect, SHG offers two advantages. First, the SHG wave couples linearly to the spontaneous polarization of the hexagonal RMnO$_3$ compounds. As Fig. S2 shows, the system size dependence of the spontaneous polarization is very weak compared to that of, e.g., $\Phi_6 = \langle\cos(6\phi)\rangle$. Second, SHG has a relatively large coherence length in the order of 10 μm which is determined by the interference of the homogeneous and the inhomogeneous solution of the wave equation at the doubled frequency[5]. These two criteria explain why finite-size

effects in the SHG experiment are negligible.

Care has to be taken that the sample is homogeneous throughout the volume coherently probed by SHG (as by any other technique; see the discussion on the neutron diffraction data in the main text). Homogeneity is perturbed by domain formation. Because of this we worked with samples close to a single-domain polarization state and suppressed domain wall movements as described above.

1. Shiozaki, Y., Nakamura, E. & Mitsui, T. (ed.) *Landolt-Börnstein Database*, $LiNbO_3$ [F] Tables 2A-1, DOI: 10.1007/10426842_395

2. Wadhawan, V. *Introduction to Ferroic Materials* (CRC Press, 2000).

3. Lottermoser, T., Lonkai, T., Amman, U., Hohlwein, D., Ihringer, J. & Fiebig, M. Magnetic phase control by an electric field. *Nature* **430**, 541 (2004).

4. Pershan, P. S. Nonlinear optical properties of solids: Energy considerations. *Phys. Rev.* **130**, 919 (1963).

5. Shen, Y. R. *The Principles of Nonlinear Optics*, (Wiley, New York, 2003).

Figure 1 Relation between SHG and ferroelectric polarization at high temperature. Temperature dependence of the SHG amplitude from a $LiNbO_3$ single crystal in comparison to the expected scaling of the spontaneous polarization[2] $P_s \propto (T_C - T)^{0.5}$. The excellent match shows that the SHG amplitude is scaling solely with the spontaneous polarization.

Figure 2 Comparison of finite-size effects. MC-simulated temperature dependence of the discreteness parameter Φ_6 and of the spontaneous polarizetion P_s. Systems of two different sizes, $L = 8$ and $L = 24$, are compared, where L can be associated to the coherence length of the experimental technique used for probing the system. Φ_6 shows a pronounced dependence on the system size L and reveals its strongest changes around $T^*/T_C = 0.8$ ($L = 24$) and $T^*/T_C = 0.6$ ($L = 8$). In contrast, P_s and the associated SHG amplitude are almost independent of L and reveal the actual phase transition temperature at $T/T_C = 1$.

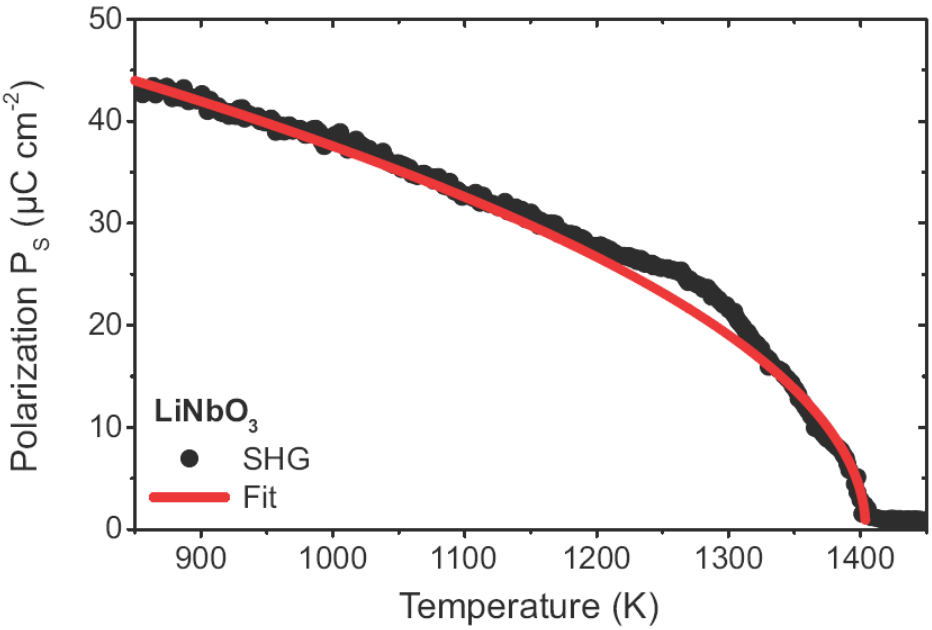
Polarization P_S (μC cm^{-2})
50
40
30
20
10
0
900
1000
1100
1200
1300
1400
Temperature (K)
LiNbO$_3$
SHG
Fit

Figure S1

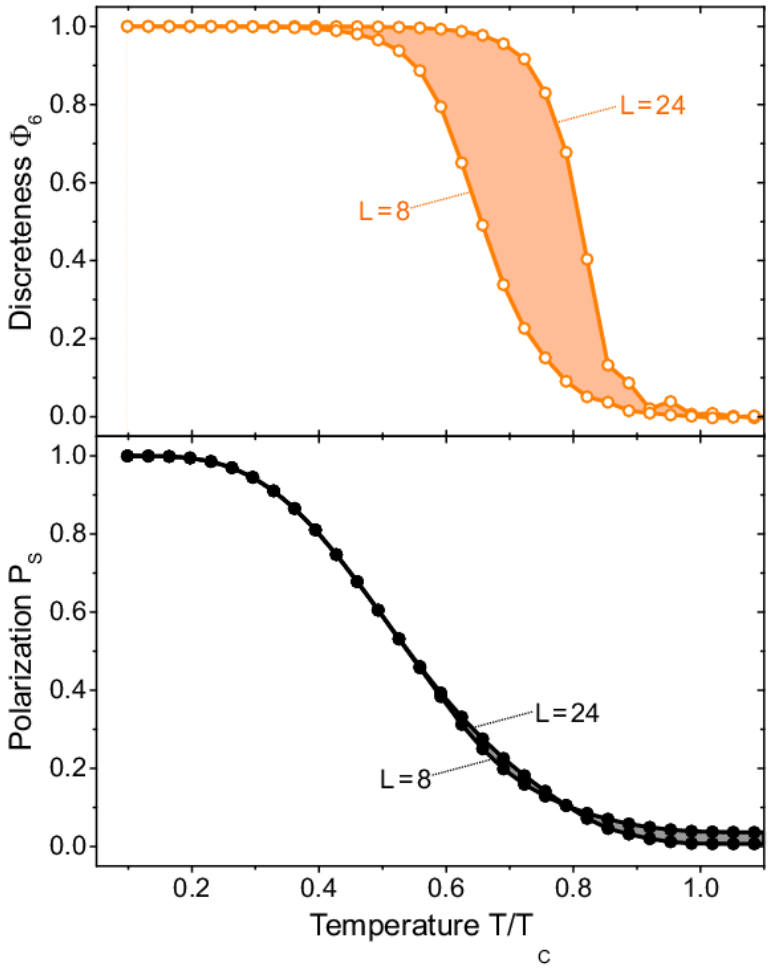
Discreteness Φ_6
1.0
0.8
0.6
0.4
0.2
0.0
L=24
L=8
Polarization P_S
1.0
0.8
0.6
0.4
0.2
0.0
L=24
L=8
0.2
0.4
0.6
0.8
1.0
Temperature T/T_C

Figure S2